PROCEEDINGS A

royalsocietypublishing.org/journal/rspa

Research

Cite this article: Basu HS, Bahga SS, Kondaraju S. 2020 A fully coupled hybrid lattice Boltzmann and finite difference method-based study of transient electrokinetic flows. *Proc. R. Soc. A* **476**: 20200423.
http://dx.doi.org/10.1098/rspa.2020.0423

Received: 29 May 2020
Accepted: 17 September 2020

Subject Areas:
mechanical engineering, fluid mechanics

Keywords:
electrokinetic instabilities, lattice Boltzmann method, finite difference method, hybrid model

Author for correspondence:
Sasidhar Kondaraju
e-mail: sasidhar@iitbbs.ac.in

A fully coupled hybrid lattice Boltzmann and finite difference method-based study of transient electrokinetic flows

Himadri Sekhar Basu[1], Supreet Singh Bahga[2] and Sasidhar Kondaraju[1]

[1]School of Mechanical Sciences, Indian Institute of Technology Bhubaneswar, Khordha, Odisha 752050, India
[2]Department of Mechanical Engineering, Indian Institute of Technology Delhi, Hauz Khas, New Delhi 110016, India

HSB, 0000-0001-6609-3033; SK, 0000-0002-3932-3494

Transient electrokinetic (EK) flows involve the transport of conductivity gradients developed as a result of mixing of ionic species in the fluid, which in turn is affected by the electric field applied across the channel. The presence of three different coupled equations with corresponding different time scales makes it difficult to model the problem using the lattice Boltzmann method (LBM). The present work aims to develop a hybrid LBM and finite difference method (FDM)-based model which can be used to study the electro-osmotic flows (EOFs) and the onset of EK instabilities using an Ohmic model, where fluid and conductivity transport are solved using LBM and the electric field is solved using FDM. The model developed will be used to simulate three different problems: (i) EOF with varying zeta-potential on the wall, (ii) similitude in EOF, and (iii) EK instabilities due to the presence of conductivity gradients. Problems (i) and (ii) will be compared with the analytical results and problem (iii) will be compared with the simulations of a spectral method-based numerical model. The results obtained from the present simulations will show that the developed model is capable of studying transient EK flows and of predicting the onset of instability.

Electronic supplementary material is available online at https://doi.org/10.6084/m9.figshare.c.5173288.

THE ROYAL SOCIETY PUBLISHING

1. Introduction

Electric field-driven fluid flows are widely used in microfluidic systems for pumping fluids [1–3] and for solute transport [4,5]. These flows result when the free charge in fluid couples with an externally applied electric field to apply an electric body force on the fluid. Such coupling of free charge and electric field occurs in the electric double layer (EDL) that forms in an electrolyte near a charged microchannel surface and drives an electro-osmotic flow (EOF) [1]. However, compared with the characteristic length scale of 10 µm or greater of a typical microchannel flow, the typical thickness of an EDL is a few tens of nanometres. In contrast to such a charge accumulation in the EDL near a solid surface, a free charge can also occur in the bulk solution when an electric field is applied through an electrolyte with a gradient in electrical conductivity [6]. On the application of an external electric field, these free charges drive the bulk flow. Such flow phenomena are caused by the balance between electric and viscous forces and are termed electroviscous flow. When the applied electric field is beyond a critical value, instabilities arise in the flow. Such instabilities are called electrohydrodynamic (EHD) instabilities [6–8]. In microfluidic systems, EHD instabilities are invariably coupled with EOF, and the resulting instabilities are termed electrokinetic (EK) instabilities [9–12].

EK flows in microfluidic systems can range from simple one-dimensional steady flows, such as plug-shaped EOF in a straight channel, to chaotic multi-dimensional EK instabilities [13]. While analytical solutions exist for steady EK flows in simplified geometries, the analysis of steady and unsteady EK flows in complex geometries requires numerical simulations. Examples of steady multi-dimensional EK flows include EOF at the junction of a microfluidic network [14] and EOF due to an axially varying surface charge [4]. On the other hand, examples of unsteady multi-dimensional EK flows include EK instability in a micromixer [12,15,16] and instability due to the conductivity gradient in electrophoresis [17–19]. Because of the complex nature of such flows, experimental measurements of local electric field and pressure distribution are not possible within a microchannel. Moreover, the accuracy of flow measurement techniques such as micro-particle image velocimetry is limited for EK flows because of the inconsistent electrophoretic mobility of seeding particles [20]. Hence, numerical simulations are inevitable in understanding EK flows.

Multi-dimensional simulations of EOF were first performed by Patankar & Hu [14]. They presented steady, three-dimensional (3D) simulations of EOF in a cross-channel geometry. These simulations were based on a finite volume scheme with a semi-implicit method for pressure-linked equations revised (SIMPLER) algorithm. Since then, a variety of simulations of EOF in microfluidic devices based on conventional computational fluid dynamics (CFD) techniques have been reported [21–23]. However, these simulation studies did not involve EK instabilities that arise from the interaction between conductivity gradients and an electric field. Lin *et al.* [9] were the first to present unsteady, two-dimensional (2D) numerical simulations of EK instability, wherein the coupled effects of electro-osmotic and electroviscous flows were accounted for. Lin *et al.* used a pseudo-spectral method to simulate EK instability with an orthogonal conductivity gradient and electric field. Thereafter, Storey [24] and Santos & Storey [19] extended this model to three dimensions to simulate EK instabilities in various flow configurations. Unsteady simulations of EK instability in cross-shaped microchannels have also been presented by Luo [25] and Li *et al.* [26] using the finite difference method (FDM).

The majority of the previous studies on simulations of EK flows are based on solving the continuum governing equations using conventional CFD techniques such as finite difference, finite element, finite volume and spectral methods. Attempts to simulate EK flows using the lattice Boltzmann method (LBM) have also been reported in the literature [27–31]. LBM is an upcoming CFD tool, with the benefits of easy implementation of parallel computing and boundary conditions (BCs) and hassle-free treatment of nonlinear terms [32–34]. These features make LBM a competitive simulation tool for complicated nonlinear problems such as micro-scale unsteady EK flows. Hlushkou *et al.* [27] used LBM to solve fluid transport equations for 3D EOF in porous media, while the Nernst–Planck equations for species conservation [1] and the Poisson equation for electric potential were solved using the FDM. Wang & Kang [29] and

Yoshida *et al.* [30] presented simulations of EOF using LBM for all the governing equations, which include the Navier–Stokes, Poisson and Nernst–Planck equations. While simulations by Wang & Kang [29] were limited to steady EOF, Yoshida *et al.* [30] presented simulations of transient EOF. All numerical studies on electric field-driven flows using LBM are limited only to EOF. Until now the use of LBM has not been demonstrated for simulating complex, unsteady EK instabilities that arise from the coupling of conductivity gradients and an electric field in a bulk solution.

In the present work, we develop a *hybrid* model based on LBM and FDM to study transient EK flows with homogeneous and heterogeneous conductivity. Unlike Wang & Kang [29] and Yoshida *et al.* [30], we solve equations for the Ohmic model [12] under thin EDL conditions to simulate transient EK flows instead of the Poisson–Nernst–Planck equations. The advantage of the Ohmic model lies in the reduction of the computational cost when the electrolyte consists of single anionic and cationic species. Such a binary-electrolyte model has also been used for predicting electrodeposition [35,36]. The Ohmic model equations involve the Navier–Stokes equation with an electric body force to solve fluid transport, an advection–diffusion-based equation to solve for the conductivity field and a steady Ohm's law to solve for the electric potential. Compared with previous LBM-based advection–diffusion equations [37–40], the present problem is challenging because of significantly different time scales for fluid and conductivity transport. Such a difference in time scales puts a constraint on the non-dimensional relaxation time while modelling unsteady EK flows using LBM on the same lattice. A further complication arises from the coupling of the fluid and conductivity equations through the convective terms.

The numerical model that we present here resolves the aforementioned issue of widely different time scales involved in unsteady EK flows. We hybridize our model by solving fluid and conductivity transport using LBM and Ohm's law using FDM on the same lattice. The Poisson equation, being a time-independent equation, can be solved efficiently using a steady-state FDM approach rather than the transient LBM approach. Such a hybridization of schemes has been reported for coupled nonlinear simulations and is often applied for problems with a large difference in length scales, as in aerodynamics and climate science, to increase computational efficiency [41–44]. Also, at the micro-scale, hybrid schemes have been successfully applied for problems like emulsification and heat transfer with surfactants [45–47].

This article is organized as follows. In §2, we review the governing equations for unsteady EK flows. In §3, we present the numerical method along with the algorithm. Finally, in §4, we present the results obtained from our hybrid numerical scheme and verify them with analytical and numerical solutions available in the literature.

2. Mathematical formulation and boundary condition

Equations governing EK flows are well discussed by many authors [9,11,24,29]. Lin *et al.* [9] have elaborated the transformation of Ohm's law (equation (2.3)) and conductivity transport (equation (2.4)) from simplified ion-transport equations considering a symmetric binary electrolyte. They further assumed a thin EDL and electroneutrality of the bulk to derive the non-dimensional form of the governing equations [48]. We present the dimensionless form of the governing equations for the present numerical scheme as

$$\nabla \cdot \mathbf{u} = 0, \tag{2.1}$$

$$\frac{Ra_e}{Sc}\left(\frac{\partial \mathbf{u}}{\partial t} + \mathbf{u} \cdot \nabla \mathbf{u}\right) = -\nabla p + \nabla^2 \mathbf{u} + \nabla^2 \phi \nabla \phi, \tag{2.2}$$

$$\nabla \cdot (\sigma \nabla \phi) = 0 \tag{2.3}$$

and

$$\frac{\partial \sigma}{\partial t} + \mathbf{u} \cdot \nabla \sigma = \frac{1}{Ra_e} \nabla^2 \sigma. \tag{2.4}$$

In these equations, $\mathbf{u}$, p, ϕ and σ represent the dimensionless velocity, pressure, electric potential and electrical conductivity, respectively. Ra_e and Sc are the electric Rayleigh number

royalsocietypublishing.org/journal/rspa Proc. R. Soc. A 476: 20200423

and Schmidt number, respectively, and are expressed as a ratio of two time scales as

$$Ra_e \equiv \frac{\tau_d}{\tau_{\rm ev}} = \frac{\epsilon E_a^2 H^2}{\mu D_{\rm eff}} \tag{2.5a}$$

and

$$Sc \equiv \frac{\tau_d}{\tau_\nu} = \frac{\mu}{\rho D_{\rm eff}}, \tag{2.5b}$$

where E_a and H are the scaling parameters for the electric field and length, respectively. ϵ, μ, ρ and $D_{\rm eff}$ denote the absolute permittivity, dynamic viscosity, density of solution and effective diffusivity of the ionic species, respectively. τ_d, $\tau_{\rm ev}$ and τ_ν are the time scales for molecular diffusion, electroviscous convection and momentum diffusion, respectively. Another time scale, $\tau_{\rm eo}$, is associated with electro-osmotic transport. These time scales have the mathematical form of

$$\tau_\nu \equiv \frac{\rho H^2}{\mu}, \tag{2.6a}$$

$$\tau_d \equiv \frac{H^2}{D_{\rm eff}}, \tag{2.6b}$$

$$\tau_{\rm eo} \equiv \frac{H}{U_{\rm eo}} = -\frac{\mu H}{\epsilon E_a \zeta} \tag{2.6c}$$

and

$$\tau_{\rm ev} \equiv \frac{H}{U_{\rm ev}} = \frac{\mu}{\epsilon E_a^2}, \tag{2.6d}$$

where ζ represents the wall ζ-potential. The electroviscous velocity ($U_{\rm ev}$) and electro-osmotic velocity ($U_{\rm eo}$) are the scaling parameters for fluid velocity for the cases of EK instability and EOF, respectively, and are defined as

$$U_{\rm ev} \equiv \frac{\epsilon E_a^2 H}{\mu} \tag{2.7a}$$

and

$$U_{\rm eo} \equiv -\frac{\epsilon \zeta E_a}{\mu}. \tag{2.7b}$$

For electroviscous cases, Re (Reynolds number) and R_ν are two other non-dimensional numbers that govern EK transport and can be mathematically written as

$$Re \equiv \frac{\tau_\nu}{\tau_{\rm ev}} = \frac{\rho \epsilon E_a^2 H^2}{\mu^2} \tag{2.8a}$$

and

$$R_\nu \equiv \frac{\tau_{\rm eo}}{\tau_{\rm ev}} = -\frac{E_a H}{\zeta}. \tag{2.8b}$$

For electro-osmotic transport, Re is given as the ratio of τ_ν to $\tau_{\rm eo}$

$$Re \equiv \frac{\tau_\nu}{\tau_{\rm eo}} = -\frac{\rho \epsilon \zeta E_a H}{\mu^2}. \tag{2.9}$$

While the equations for fluid transport (equations (2.1)–(2.2)) are accompanied by a no-slip condition on solid walls for EHD cases as

$$\mathbf{u} \cdot \hat{t}_\parallel = 0, \tag{2.10}$$

in EK instability, we assume electro-osmotic slip on solid walls, which is tangential to the wall. This slip velocity is given as

$$\mathbf{u} \cdot \hat{t}_\parallel = \frac{1}{R_\nu} \zeta \mathbf{E} \cdot \hat{t}_\parallel. \tag{2.11}$$

Here, $\mathbf{E}$ represents the electric field at the boundary. Normal velocity vanishes at solid, non-porous boundaries and can be mathematically written as

$$\mathbf{u} \cdot \hat{n}_\perp = 0. \tag{2.12}$$

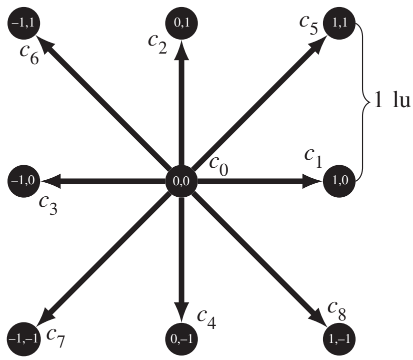

Figure 1. Number convention used for lattice velocity directions for the D2Q9 velocity models used in this article.

BCs for electric potential (equation (2.3)) and electrical conductivity (equation (2.4)) are prescribed [9] as

$$\nabla\phi \cdot \hat{n}_\perp = 0 \tag{2.13}$$

and

$$\nabla\sigma \cdot \hat{n}_\perp = 0. \tag{2.14}$$

Here, $\hat{t}_\parallel$ and $\hat{n}_\perp$ are unit vectors pointing to the tangential and normal directions with respect to the wall, respectively. The assumption that the solid surface is non-conductive and hence the potential gradient is absent at the solid–liquid interface is represented by equation (2.13). Similarly, equation (2.14) indicates that there is no ion diffusion across the boundaries and, therefore, the conductivity gradient is absent at the solid surface [48]. More detailed information on BCs can be found in Lin *et al.* [9] and Santos & Storey [19].

3. Numerical method

In this study, we employ a fully coupled hybrid lattice Boltzmann–finite difference (LB-FD) method-based scheme to solve the governing equations in the modified binary electrolyte model provided by Lin *et al.* [9,49]. We solve fluid (equations (2.1) and (2.2)) and electrical conductivity (equation (2.4)) transport equations in LBM. Ohm's law (equation (2.3)) has the form of a Poisson equation where the source term is a function of the dependent variable itself. For such an equation, we apply a second-order central difference scheme to discretize and a successive over-relaxation (SOR) scheme to solve the discrete equation. LBM has been extensively used as a tool to simulate fluid and similar transport equations at the mesoscale [39,46,47,50]. Unlike conventional CFD, it solves the mesoscale Boltzmann equations to obtain macroscopic variables such as fluid density, velocity, temperature, ion concentration and other properties by tracking the distribution functions of species packets on lattices. In our 2D simulations, we use the D2Q9 scheme (figure 1) for lattice velocity directions. In the rest of this section, we shall discuss the evolution equations needed to solve equations (2.1), (2.2) and (2.4) in LBM; discretization and the scheme used in FDM for equation (2.3); the formulation of BCs in LBM; and the algorithm of the proposed numerical model.

(a) Evolution equations

Partial differential equations like Navier–Stokes equations and advection–diffusion equations can be recovered from discrete Boltzmann equations through several schemes in LBM [32,33], such as the multi-relaxation time (MRT), two-relaxation time, entropic LBM and single relaxation time (SRT) [51]. While SRT–LBM, also known as the single collision model or BGK model, is known to have stability issues for high Mach number flows, it provides simplicity and computational efficiency. Moreover, the BGK model provides satisfactory performance for the instability physics within the onset regime. Hence we consider SRT–LBM to solve fluid and electrical conductivity transport equations. In this work, we solve all the governing equations on the same set of lattices or grids.

(i) Evolution equation for fluid transport

The evolution equation for incompressible, laminar flow with an external force has the form [32,33]

$$f_a(\mathbf{x}+\mathbf{c}_a\Delta t_f, t+\Delta t_f) = f_a(\mathbf{x}, t) - \frac{f_a(\mathbf{x}, t) - f_a^{\mathrm{eq}}(\mathbf{x}, t)}{\tau_f} + F_a \Delta t_f, \tag{3.1}$$

where f_a, $\mathbf{x}$, $\mathbf{c}_a$, Δt_f and τ_f denote the packet distribution function in the direction of a, the position vector, the discrete lattice velocity in the direction of a, the lattice time step for fluid evolution and the dimensionless relaxation time, respectively. F_a denotes the external force in the direction of a. In the D2Q9 model, the discrete velocities are

$$[\mathbf{c}_0, \mathbf{c}_1, \mathbf{c}_2, \mathbf{c}_3, \mathbf{c}_4, \mathbf{c}_5, \mathbf{c}_6, \mathbf{c}_7, \mathbf{c}_8] = \begin{bmatrix} 0 & 1 & 0 & -1 & 0 & 1 & -1 & -1 & 1 \\ 0 & 0 & 1 & 0 & -1 & 1 & 1 & -1 & -1 \end{bmatrix}. \tag{3.2}$$

The equilibrium distribution function f_a^{eq} for fluid flow [32] is defined as

$$f_a^{\mathrm{eq}}(\mathbf{x}, t) = \omega_a \rho(\mathbf{x}, t) \left[1 + 3\frac{\mathbf{c}_a \cdot \mathbf{u}}{c^2} + \frac{9}{2}\frac{(\mathbf{c}_a \cdot \mathbf{u})^2}{c^4} - \frac{3}{2}\frac{\mathbf{u}^2}{c^2}\right], \tag{3.3}$$

with

$$\omega_a = \begin{cases} \dfrac{4}{9} & \text{for} \quad a = 0, \\ \dfrac{1}{9} & \text{for} \quad a = 1-4, \\ \dfrac{1}{36} & \text{for} \quad a = 5-8. \end{cases} \tag{3.4}$$

Here, c represents the lattice speed and is defined as $c = \Delta x/\Delta t_f$, where Δx is the lattice distance. For simplicity, Δx and Δt_f are considered as unity in lattice units for fluid transport, thus leading to $c = 1$.

The relaxation time for the fluid evolution equation is calculated from the fluid viscosity in lattice units by

$$\tau_f = 3\nu + \tfrac{1}{2}. \tag{3.5}$$

We consider the value of the relaxation time to be $1/2 < \tau_f \leq 2$ owing to the stability criteria for LBM [32]. We choose the value of τ_f accordingly, considering the coupling with the electrical conductivity transport equation. For EK flows in a microchannel, the force term due to the application of an external electric field in the discrete LB equation [29,33,37] is given as

$$F_a = \frac{3\rho_e \mathbf{E} \cdot (\mathbf{c}_a - \mathbf{u})}{\rho c^2} f_a^{\mathrm{eq}}, \tag{3.6}$$

where ρ, $\mathbf{u}$, $\mathbf{E}$ and ρ_e are the macroscopic density, velocity, electric field and charge density, respectively, in lattice units. From the population distribution considering the low Mach number limit, the macroscopic variables density and velocity are recovered as

$$\rho = \sum_a f_a \tag{3.7}$$

and

$$\mathbf{u} = \frac{1}{\rho}\sum_a \mathbf{c}_a f_a. \tag{3.8}$$

(ii) Evolution equation for electrical conductivity transport

Electrical conductivity transport (equation (2.4)) is an advection–diffusion equation similar to energy transport. Solutions for such scalar transport equations using LBM have been reported

royalsocietypublishing.org/journal/rspa Proc. R. Soc. A 476: 20200423

in [37,51]. Hence we follow a similar procedure to solve the conductivity transport equation (see the electronic supplementary material for a Chapman–Enskog analysis of the discrete LBE). The evolution equation to solve the electrical conductivity transport equation has the form

$$g_a(\mathbf{x}+\mathbf{c}_a\Delta t_c, t+\Delta t_c) = g_a(\mathbf{x},t) - \frac{g_a(\mathbf{x},t) - g_a^{\mathrm{eq}}(\mathbf{x},t)}{\tau_{D_{\mathrm{eff}}}}, \tag{3.9}$$

where discrete velocities ($\mathbf{c}_a$) are the same as discussed in fluid evolution. g_a represents the distribution function for electrical conductivity. Δt_c denotes the lattice time step for conductivity transport and is considered unity for simplicity. The relaxation time $\tau_{D_{\mathrm{eff}}}$ for this equation is calculated using

$$\tau_{D_{\mathrm{eff}}} = 3D_{\mathrm{eff}} + \tfrac{1}{2}. \tag{3.10}$$

We follow the same convention as discussed in fluid evolution and choose the value of the relaxation time as $1/2 < \tau_{D_{\mathrm{eff}}} \leq 2$ owing to the stability criterion. Because of the difference in time scale between fluid and conductivity transport, such a value of the relaxation parameter results in higher diffusion, leading to stability of the scheme. However, such a diffusion is not high enough to alter the physics of the EK instability itself. The expression for the equilibrium distribution function g_a^{eq} for electrical conductivity is assumed to be the same as that used in LBM for energy transport [33] and can be written as

$$g_a^{\mathrm{eq}}(\mathbf{x},t) = \omega_a\sigma(\mathbf{x},t)\left[1 + 3\frac{\mathbf{c}_a \cdot \mathbf{u}}{c^2}\right], \tag{3.11}$$

where the weight function ω_a in g_a^{eq} is the same as discussed in fluid evolution. Under a low Mach number limit, such a linear relation of g_a^{eq} is sufficient to recover the macroscopic scalar property from the population distribution [51]. The lattice speed $c = \Delta x/\Delta t_c = 1$ considering Δt_c as unity in lattice units for conductivity transport. Similar to fluid evolution, the macroscopic electrical conductivity is recovered from

$$\sigma = \sum_a g_a. \tag{3.12}$$

(iii) Evolution equation for Ohm's law

Expanding the equation for Ohm's law (equation (2.3)), we get

$$\sigma\nabla^2\phi + \nabla\sigma \cdot \nabla\phi = 0. \tag{3.13}$$

Discretization using a second-order central difference scheme of this equation for 2D models yields

$$\begin{aligned}\sigma_{i,j}&\left[\frac{\phi_{i+1,j} - 2\phi_{i,j} + \phi_{i-1,j}}{\Delta x^2} + \frac{\phi_{i,j+1} - 2\phi_{i,j} + \phi_{i,j-1}}{\Delta y^2}\right]\\ &+\left[\frac{\sigma_{i+1,j} - \sigma_{i-1,j}}{2\Delta x} \cdot \frac{\phi_{i+1,j} - \phi_{i-1,j}}{2\Delta x} + \frac{\sigma_{i,j+1} - \sigma_{i,j-1}}{2\Delta y} \cdot \frac{\phi_{i,j+1} - \phi_{i,j-1}}{2\Delta y}\right] = 0.\end{aligned} \tag{3.14}$$

In explicit form assuming $\Delta x = \Delta y = 1$, we obtain

$$\begin{aligned}\phi_{i,j} = &\frac{1}{4}\left[\phi_{i+1,j} + \phi_{i-1,j} + \phi_{i,j+1} + \phi_{i,j-1}\right]\\ &+ \frac{1}{16\sigma_{i,j}}\left[(\sigma_{i+1,j} - \sigma_{i-1,j})(\phi_{i+1,j} - \phi_{i-1,j}) + (\sigma_{i,j+1} - \sigma_{i,j-1})(\phi_{i,j+1} - \phi_{i,j-1})\right].\end{aligned} \tag{3.15}$$

From equation (3.15), we calculate ϕ using a SOR scheme [52] as

$$\phi_{i,j}^{k+1} = (1-w)\phi_{i,j}^{k} + w\phi_{i,j}^{k+1'}, \tag{3.16}$$

where w represents the relaxation factor, and k and $k+1$ are the previous and present iteration steps, respectively.

(b) Implementation of boundary conditions

(i) Boundary treatment for fluid transport

For simulations of EOF, the fluid evolution equation (equation (3.1)) is accompanied by a slip velocity tangential to the solid boundary. We consider zero velocity in the wall-normal direction and apply the Neumann BC on a solid wall for the fluid evolution equation (equation (3.1)) [32]. To calculate unknown distributions at a solid wall from the prescribed velocities and known local distribution functions an on-grid approach prescribed by Zou & He [53] has been adopted. Considering a horizontal bottom wall in a flow between parallel plates, for example, the populations f_1, f_3, f_4, f_7 and f_8 are known from the previous streaming step. The unknown distributions f_2, f_5 and f_6 are calculated as

$$u = -\frac{\epsilon \zeta E_x}{\mu}, \tag{3.17a}$$

$$v = 0, \tag{3.17b}$$

$$\rho = f_0 + f_1 + f_3 + 2 \times (f_4 + f_7 + f_8), \tag{3.17c}$$

$$f_2 = f_4 + \frac{2}{3}\rho v, \tag{3.17d}$$

$$f_5 = f_7 - \frac{1}{2}(f_1 - f_3) + \frac{1}{2}\rho u + \frac{1}{6}\rho v \tag{3.17e}$$

and

$$f_6 = f_8 + \frac{1}{2}(f_1 - f_3) - \frac{1}{2}\rho u + \frac{1}{6}\rho v, \tag{3.17f}$$

where E_x is the tangential component of the electric field at the wall in the lattice unit. u and v represent the tangential and normal components of the velocity at the wall in the lattice unit, respectively.

(ii) Boundary treatment for electrical conductivity transport

We prescribe a no-flux BC on solid walls for the electrical conductivity transport equation (equation (3.9)), similar to that used in LBM for scalar transport problems [33,38,40]. To apply a no-flux condition in LBM, we equate all the distributions except f_0 on a solid node to the adjacent fluid node. For example, if we consider nodes $(i, 0)$ and $(i, j+1)$ on the horizontal bottom and top walls, respectively, BCs are applied as

$$g_a(i, 0) = g_a(i, 1) \tag{3.18a}$$

and

$$g_a(i, j+1) = g_a(i, j), \tag{3.18b}$$

where $a = 1, 2, \ldots, 8$.

(iii) Boundary treatment for Ohm's law

In FDM, a no-flux BC is applied by equating the variable value from the computational domain to the boundary [52]. Considering a solid wall at $y = 0$, and $y = j + 1$, BCs are applied on the bottom and top wall, respectively, as

$$\phi(i, 0) = \phi(i, 1) \tag{3.19a}$$

and

$$\phi(i, j+1) = \phi(i, j). \tag{3.19b}$$

(c) Algorithm for the present numerical model

The discretized equations (equations (3.1), (3.9) and (3.15)) are coupled together, and each problem involves different time scales. As previously mentioned, for simplicity, the lattice

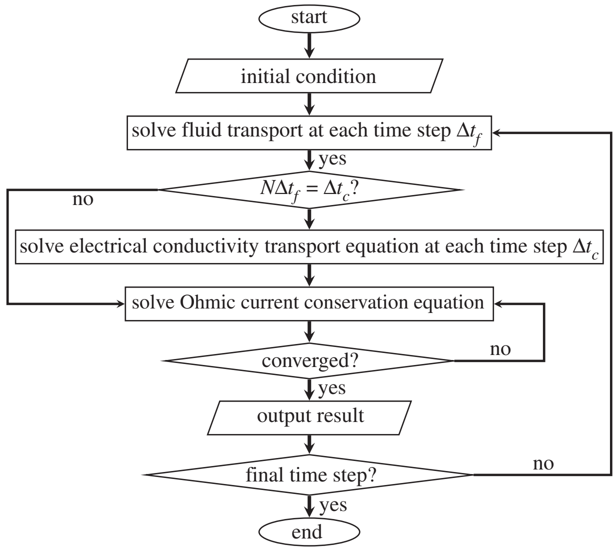

Figure 2. Algorithm for the present model.

distance (Δx) and lattice time-step (Δt) have been assumed to have unity. Physical units (e.g. kg, m, sec, A) are scaled to lattice units in such a way that the condition $1/2 < \tau_f \leq 2$ is satisfied. For example, the kinematic viscosity of value 10^{-6} m^2 s^{-1} is converted to value 0.4 in lattice units, which in turn gives a relaxation time of 1.7 using equation (3.5) (refer to the electronic supplementary material). Similar steps are followed for the conductivity equation.

Figure 2 illustrates the algorithm for the present hybrid numerical model. The three differential equations simultaneously solved in this article have different time scales. While Ohm's law (equation (2.3)) is a steady-state equation, the ratio of time scales for the fluid transport equation (equation (2.2)), τ_ν, to the electrical conductivity transport equation (equation (2.4)), τ_d, is of the order of 10^{-3}. To resolve this anomaly in time scales, N number of time iterations for the fluid evolution equation are performed (equation (3.1)) for each time iteration of the electrical conductivity evolution equation (equation (3.9)), where $N = \Delta t_c/\Delta t_f$ is a positive integer and Δt_c and Δt_f are in physical units (refer to the electronic supplementary material for typical values of N). We perform spatial iterations for the discrete Ohmic equation (equation (3.15)) at each time step of the fluid evolution equation.

In the present simulations, the first fluid evolution equation (equation (3.1)) is solved using the initial condition to obtain the velocities. Since the fluid and electrical conductivity evolution equations use different lattice time units, these velocities are converted to lattice units for electrical conductivity. Then these velocity values are used to solve the electrical conductivity evolution equation (equation (3.9)) to obtain the values of electrical conductivity in the domain. Ohm's law is coupled with the conductivity equation through electrical conductivity and uses the same lattice units as that of electrical conductivity. By solving the discretized form of Ohm's law (equation (3.15)), we obtain the electric potential. The governing equation for fluid flow is coupled to Ohm's law through the electric body force. Hence, the values of electric potential are converted to lattice units for fluid evolution, which are then used to calculate the force term in the fluid evolution equation.

4. Validation and discussion

To validate our numerical model, we present simulations of various EK flow problems and compare the results obtained with analytical and numerical solutions available in the literature. First, we consider the case of EOF with sinusoidal variation in the ζ-potential at the microchannel

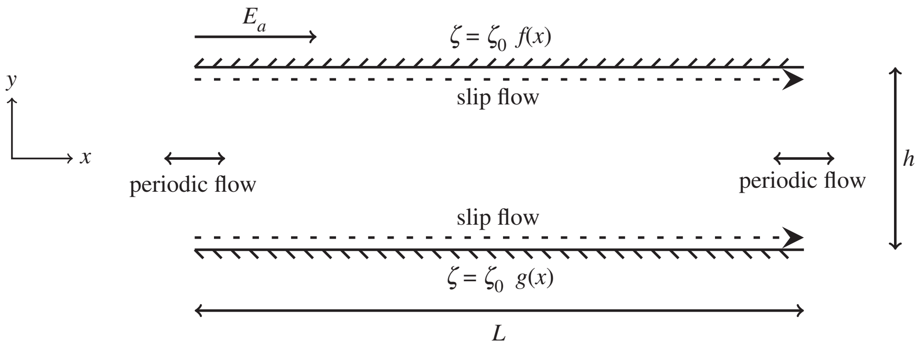

Figure 3. Schematic for EOF with variable ζ-potential. Slip flow is assumed at the solid wall. In these simulations, we assume sinusoidal variation of the charge density at the wall, which creates a sinusoidal ζ-potential at the wall. $h = 25\ \mu\text{m}$, $L = 500\ \mu\text{m}$, $qh = 0.314$.

wall. A solution to such problems can be obtained analytically [54,55]. Thereafter, we show the similitude between electric field lines and streamlines in EOF in a cross-channel geometry [56]. Finally, we simulate EK instability in a flow configuration wherein the electric field is applied along an interface separating two electro-osmotically driven fluid streams with different conductivities. The results of these simulations are compared with the DNS by Lin *et al.* [9]. For all our simulations, we assume density (ρ), kinematic viscosity (ν) and electrical permittivity (ϵ) of the solution to be $1000\ \text{kg m}^{-3}$, $10^{-6}\ \text{m}^2\ \text{s}^{-1}$ and $6.93 \times 10^{-10}\ \text{C V m}^{-1}$, respectively.

(a) Electro-osmotic flow with variable zeta-potential

First, we consider a 2D, steady EOF with uniform conductivity between two parallel walls placed at $y = \pm h/2$ with an axially varying ζ-potential, as illustrated in figure 3. Since we consider a fluid stream with uniform conductivity, there is no electric body force in the bulk. For all the cases, $qh = 0.314$, where $q = 2\pi/L$ and $h = 25\ \mu\text{m}$. Further, the flow is considered periodic along the stream-wise direction. The ζ-potential at the walls varies as $\zeta(x) = \zeta_0 f(x)$ at the top wall and $\zeta(x) = \zeta_0 g(x)$ at the bottom wall, where $\zeta_0 = -0.07\ \text{V}$. An electric field of $20\,000\ \text{V m}^{-1}$ is applied along the axial direction.

For the first case, the ζ-potential at the walls varies as $\zeta(x) = \zeta_0 \sin(qx)$ at $y = \pm h/2$. In figure 4*a*, we plot the stream function using the simulation results and analytical results, and we find that the sinusoidal variation of the ζ-potential induces an alternating electro-osmotic slip at the boundary, which results in convective rolls [54]. We further observe that, while the variations in the ζ-potential at both walls are in phase, both *eddies* at a cross-section rotate opposite to each other in order to satisfy mass conservation. We quantified the deviation in stream function between the analytical solution and that obtained from our numerical model using the L_2 norm and found the error to be 1.1%.

Figure 4*b* shows the streamlines for another case, where the modular wave with a phase difference $\pi/2$ between the top and bottom boundary is simulated. For this simulation, we consider $\zeta(x) = -\zeta_0 \sin(qx)$ at $y = -h/2$ and $\zeta(x) = \zeta_0 \cos(qx)$ at $y = +h/2$. Other parameters are the same as in the first case. As the phase difference increases gradually, the position of the convective rolls shifts. For phase shift π, the eddies merge and form a straight single roll [54]. We observe similar gradual unification of rolls in figure 4*b* when the phase difference is $\pi/2$. The error in the stream function that is evaluated for this problem using the same method as before is 8.8%. Such a relatively large deviation compared with the previous case can be contributed to the numerical error involved in the calculation of the stream function using the finite difference approximation. However, the smallness of the estimated errors for both cases indicates that our scheme can simulate such problems with expected accuracy.

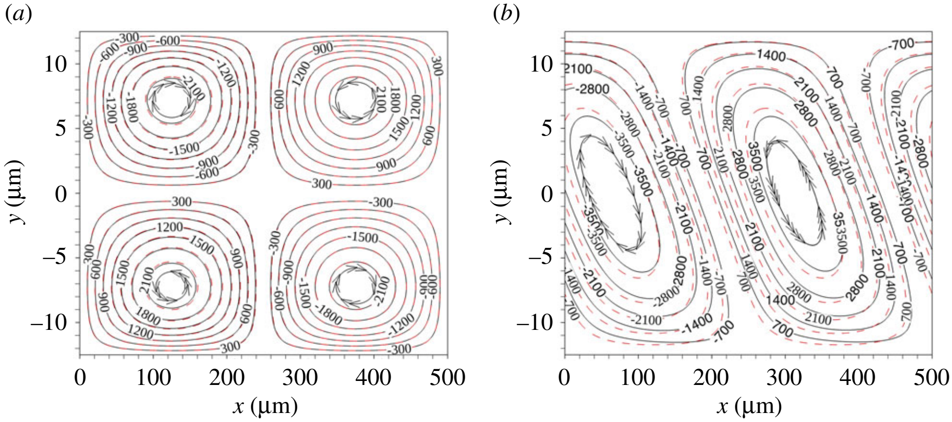

Figure 4. Streamlines from an analytical solution and simulation in $\mu m^2\,s^{-1}$. Solid black and dashed red lines represent the simulation and analytical results, respectively. (*a*) $qh = 0.314$, $\zeta(x) = \zeta_0 \sin(qx)$ at $y = \pm h/2$; (*b*) $qh = 0.314$, $\zeta(x) = -\zeta_0 \sin(qx)$ at $y = -h/2$ and $\zeta(x) = \zeta_0 \cos(qx)$ at $y = +h/2$. (Online version in colour.)

(b) Similitude of streamlines and electric field lines

The streamlines in steady EOF are known to be similar to the electric field lines provided: homogeneous fluid properties with uniform conductivity and uniform ζ-potential at the microchannel walls. Here, we simulate a 2D steady EOF of a uniform conductivity electrolyte in a cross-channel geometry with closed side-inlets. Unlike the previous problem with variable ζ-potential, an analytical solution for such a flow is unavailable owing to complex geometry and BCs. Figure 5 shows the schematic of the problem. This case is similar to the experiments of Devasenathipathy *et al.* [56] and satisfies the aforementioned conditions for similitude between the electric field and streamlines. The width (h) and length (L) of the channel are 120 and 1000 μm, respectively. The EOF is driven by an electric field that is applied by maintaining a constant electric potential of 15 V at the bottom inlet of the vertical channel and a potential of 7.5 V at the left and right ends of the horizontal channel. The outlet of the vertical channel is maintained at zero potential. The inlet and outlet of the vertical channel are assumed to be at the same pressure. Because the electric field is normal to the left and right walls of the horizontal channel, there is no tangential EOF on these walls. Hence we assume a no-slip condition at the left and the right walls of the horizontal channel. At all other channel walls, we consider an electro-osmotic slip BC for tangential velocity. All the channel walls are assumed to be impenetrable. A uniform wall ζ-potential, $\zeta_0 = -0.025\,\mathrm{V}$, is considered, resulting in the same mobility as the experimental problem stated in Devasenathipathy *et al.* [56]. Figure 6*a* shows the streamlines (black lines) and electric field lines (red lines) obtained from the present hybrid numerical simulations. As observed in figure 6*a*, streamlines and electric field lines show similarity, and qualitatively agree with the experimental results by Devasenathipathy *et al.* Further, the similarity between stream-wise velocity (u_x) and the normalized x-component of the electric field ($E_{x,\mathrm{norm}}$) at $x = 0$ can be observed from figure 6*b*. In this plot, the electric field is scaled to velocity using the Smoluchowski equation as $U_{\mathrm{eo}} = \mu_0 E_a = -\epsilon\zeta_0 E_a/\mu$, where $\mu_0 = 1.7 \times 10^{-8}\,\mathrm{m^2/Vs}$ is the mobility of the solution. The difference between u_x and $E_{x,\mathrm{norm}}$ using the L_2 norm is computed to be 2.47%. Such a small error provides the quantitative validity of our numerical model in comparison with experimental results.

(c) Electrokinetic instabilities

The previous two cases demonstrated the potential of our numerical model to simulate multi-dimensional steady EOF. However, these cases are limited to flows with homogeneous

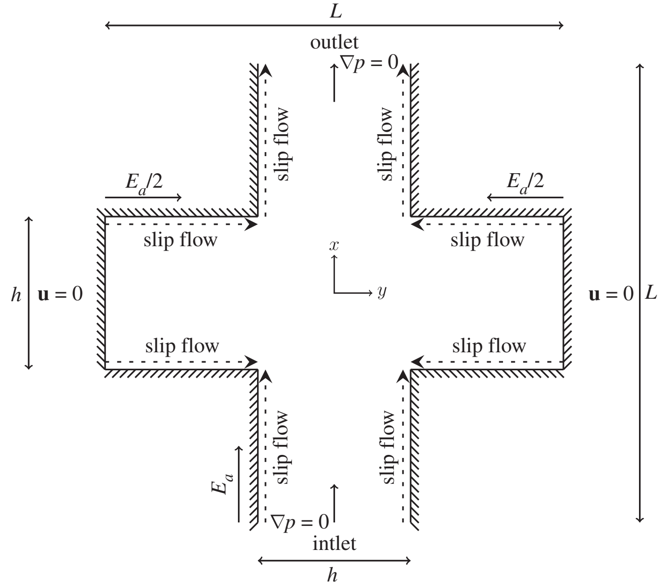

Figure 5. Schematic for the similitude problem. There is no mass flow through the side-inlets. Slip flow is assumed at the solid walls except for the closed side-inlets. Hence, both tangential and normal velocities vanish at the side-inlets. The inlet and outlet are at constant pressure. The width and length of the channel are $h = 120$ and $L = 1000$ µm, respectively. An electric field of 15 000 V m^{-1} is applied at the inlet.

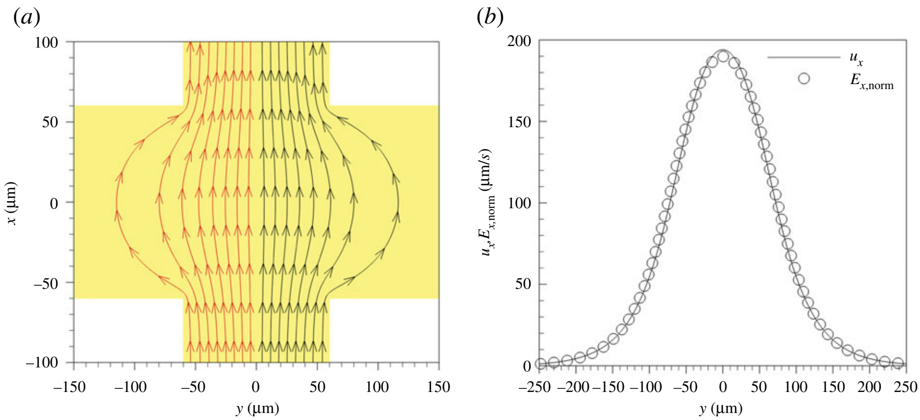

Figure 6. (*a*) Streamline and electric field lines in an EOF with uniform ζ-potential. Red (left) and black (right) lines indicate the electric field lines and streamlines, respectively. (*b*) Stream-wise velocity and the normalized x-component of the electric field in µm s^{-1}. The electric field is normalized to the velocity by using the electro-osmotic mobility. (Online version in colour.)

conductivity, wherein the electric body force in the bulk is absent. We now present simulations of a case of EK instability, which is a consequence of the conductivity gradient between two fluid streams and a coupled electric field [9,11,12,24].

Figure 7 shows a schematic of the problem and the initial conductivity contour. We consider a 2D periodic channel flow with conductivity ratio 10 : 1 and uniform ζ-potential at the walls. Red and blue colours represent the fluid streams with high and low conductivity, respectively. The parameters used for this case are the same as those in Lin *et al.* [9] except for the channel dimensions and imposed electric fields. Table 1 documents the comparative values of these parameters. Further, a random perturbation with zero mean of the order of 10^{-5} is introduced to the initial conductivity field to break the symmetry. To reduce the computational cost, channel

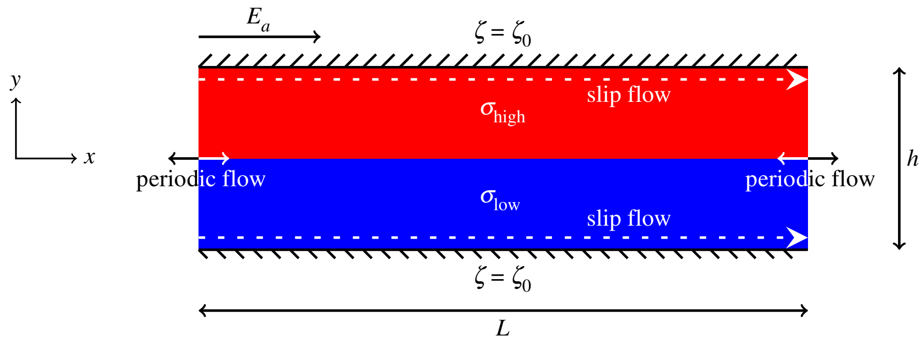

Figure 7. Schematic for EK instability simulations with an initial conductivity contour. Red (top) and blue (bottom) indicate the high and low conductivity, respectively, with a ratio of 10 : 1. The channel aspect ratio (h : L) is 1 : 4. The solid walls are 250 μm apart. Electric fields are applied towards a positive x-axis. A uniform ζ-potential of −0.07 V is applied at the walls. (Online version in colour.)

Table 1. Parameters and fundamental scales used in simulating Lin's problem.

symbol	description	present value	value from Lin *et al.*
h	height of micro-channel	250×10^{-6} m	1000×10^{-6} m
l	length of micro-channel	1000×10^{-6} m	4000×10^{-6} m
ϵ	permittivity	6.93×10^{-10} C Vm^{-1}	6.93×10^{-10} C Vm^{-1}
μ	dynamic viscosity of water	10^{-3} kg ms^{-1}	10^{-3} kg ms^{-1}
ρ_0	density for water	10^3 kg m^{-3}	10^3 kg m^{-3}
D_{eff}	effective diffusivity	2×10^{-9} m^2 s^{-1}	2×10^{-9} m^2 s^{-1}
H	length scale	125×10^{-6} m	500×10^{-6} m
C_0	molar concentration	3.3×10^{-2} mol m^{-3}	3.3×10^{-2} mol m^{-3}
σ_{low}	low conductivity	5×10^{-4} S m^{-1}	5×10^{-4} S m^{-1}
ζ_R	reference EDL ζ-potential	-7×10^{-2} V	-7×10^{-2} V
E_a	typical values for imposed field	18 000–120 000 V m^{-1}	4500–25 000 V m^{-1}
Sc	Schmidt number	500	500

dimensions are reduced in such a way that the non-dimensional numbers and channel aspect ratio are the same. The equivalent values of the electric fields and non-dimensional numbers used in both models are tabulated in table 2. Because of such scaling, the electric fields and corresponding concentration difference (δC_0) used in the present simulations are higher than their corresponding values used in DNS by Lin *et al.* [9].

To check the validity of our model on EK instability simulation, a qualitative comparison is presented in figure 8 with conductivity contours from simulations by Lin *et al.* [9] for $Ra_e = 6259$ at varying non-dimensional times (τ_{nd}), where the physical time (t) is scaled with the electroviscous time scale (τ_{ev}) to obtain τ_{nd}. As observed in the contour plots in figure 8, the conductivity fields predicted in the present simulations are similar to the results from DNS and show the capability of the present numerical model to capture the instability dynamics.

EK instability is observed when an externally applied electric field is above a specific threshold value [9,11,12]. For low electric fields below such a threshold, the diffusion of the conductivity field is dominant and suppresses the instability. In figure 9, we present the conductivity contours for different Ra_e values from the present hybrid numerical scheme. At low Ra_e, the stabilizing effect of the molecular diffusion suppresses the instability. Consequently, in the present simulations, we do not observe instability at $Ra_e = 1754$ corresponding to the electric

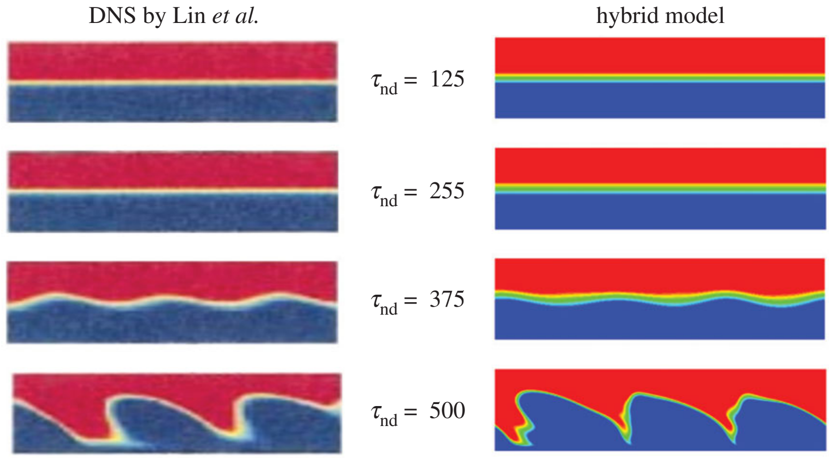

Figure 8. Comparison of conductivity contours with DNS at $Ra_e = 6259$. The $E_a = 8500\ \mathrm{V\,m^{-1}}$ case in simulations by Lin *et al.* [9] is equivalent to $E_a = 34\,000\ \mathrm{V\,m^{-1}}$ in our model owing to modification of the length scale. Left, contours from DNS; right, the results from the hybrid model. Each row represents non-dimensional time $\tau_{nd} = 125, 255, 375, 500$ from top to bottom, respectively. (Reproduced from Lin *et al.* [9], with the permission of AIP Publishing.) (Online version in colour.)

Table 2. Applied electric fields in $\mathrm{V\,m^{-1}}$ and concentration differences in $\mathrm{mol\,m^{-3}}$ in Lin *et al.* [9] and their equivalent values used for the present simulations while non-dimensional numbers are the same.

Ra_e	E_a in DNS ($\mathrm{V\,m^{-1}}$)	δC_0 in DNS ($\mathrm{mol\,m^{-3}}$)	equivalent E_a in LBM ($\mathrm{V\,m^{-1}}$)	equivalent δC_0 in LBM ($\mathrm{mol\,m^{-3}}$)
1754	4500	6.5×10^{-8}	18 000	1×10^{-6}
6259	8500	1.2×10^{-7}	34 000	2×10^{-6}
13 535	12 500	1.8×10^{-7}	50 000	2.9×10^{-6}
26 529	17 500	2.5×10^{-7}	70 000	4×10^{-6}
54 141	25 000	3.6×10^{-7}	100 000	5.7×10^{-6}

field $E_a = 18\,000\ \mathrm{V\,m^{-1}}$, whereas for $Ra_e = 6259 - 54\,141$, corresponding to electric fields $E_a =$ 34 000–100 000 $\mathrm{V\,m^{-1}}$, we observe the onset of instability at $\tau_{nd} = 400$. Therefore, the present scheme predicts that EK instability starts to appear when Ra_e is somewhere between 1754 and 6259 or higher. Hence, the threshold electric field lies between 18 000 and 34 000 $\mathrm{V\,m^{-1}}$, which is in agreement with the prediction of Lin *et al.* [9]. We also observe that the instability in the conductivity field does not start until $\tau_{nd} = 300$, which also agrees with the predictions of Lin *et al.*

At the higher electric field, the electroviscous effect results in instability [57]. As the electric field is increased, the electroviscous effect starts to overtake molecular diffusion [9]. In addition, for a stronger electric field the electroviscous effect assists in maintaining a sharper conductivity gradient with time before the onset of instability. In consequence, the instability grows at a faster rate for stronger electric fields. Such an increase in growth rate with increasing electric field is better visualized using dimensional units. Hence, conductivity contours at different electric fields for varying physical times are shown in figure 10. For $E_a = 50\,000\ \mathrm{V\,m^{-1}}$ instability appears between 0.16 s and 0.23 s, whereas the same happens between 0.08 s and 0.12 s for $E_a = 70\,000\ \mathrm{V\,m^{-1}}$. For $E_a = 100\,000\ \mathrm{V\,m^{-1}}$ flow becomes unstable much faster than in the previous cases, between 0.04 s and 0.06 s.

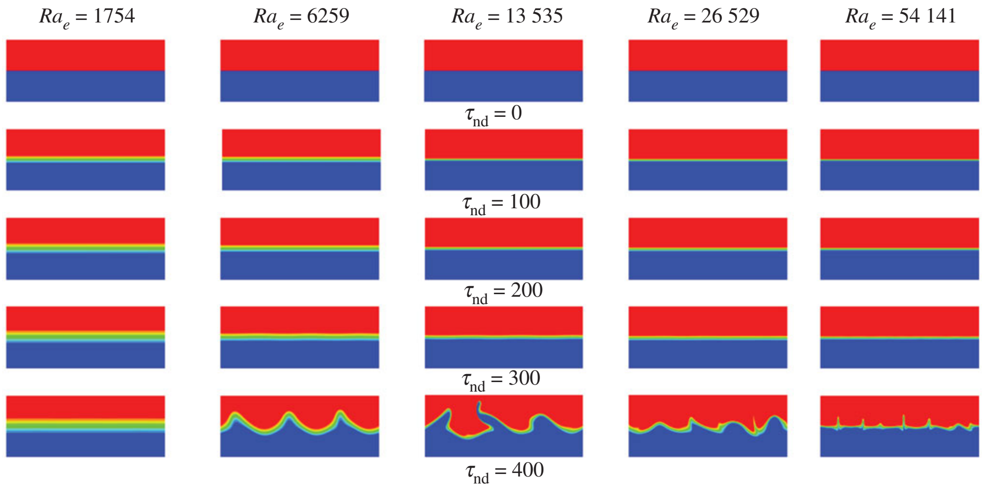

Figure 9. Conductivity contours from the hybrid model at different electric fields in terms of Ra_e. The temporal evolution of contours for each electric field is given in each column. The corresponding Ra_e is provided at the top of each column. Each row represents non-dimensional time $\tau_{\mathrm{nd}} = 0, 100, 200, 300, 400$ from top to bottom, respectively. (Online version in colour.)

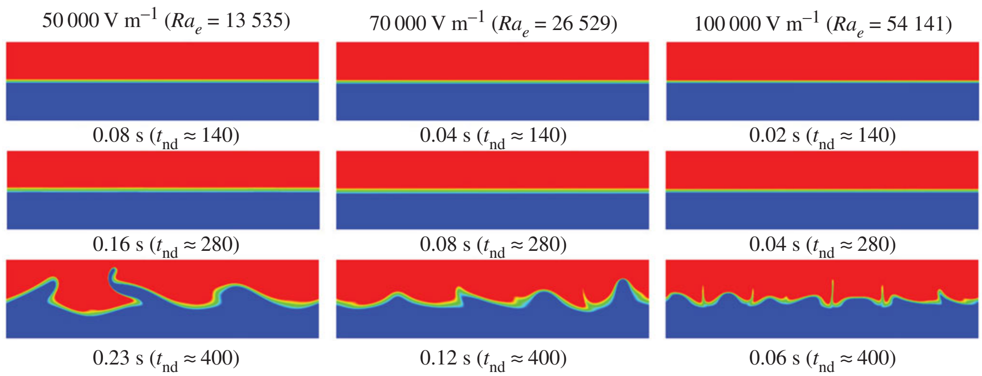

Figure 10. Dye fields for different electric fields showing faster growth of instability with increasing electric fields. (Online version in colour.)

(d) Electroviscous scaling

Contour plots in the previous section provide a qualitative comparison with DNS by Lin *et al.* [9]. To quantify electroviscous effects and check the validity of existing scaling laws under the unstable regime, we present velocity plots for varying time and electric Rayleigh number from the present simulations.

Figure 11 shows the stream-wise velocity at $\tau_{\mathrm{nd}} = 100$ and $\tau_{\mathrm{nd}} = 400$ for different Ra_e at an axial distance of 200 µm away from the inlet. Initially, the fluid in bulk moves as a result of the electro-osmotic effects, and we observe a plug flow similar to EOF [58] for all electric fields, as shown in figure 11*a*. With the increase in time, electroviscous forces start to dominate the bulk fluid motion over electro-osmotic forces. Consequently, we observe the peak of stream-wise velocities occurring at the interface of the high and low conductivities, as shown in figure 11*b*. Cross-stream distance between these peaks in bulk flow represents the thickness of the diffusive interface. For a stronger electric field, a larger conductivity gradient is maintained; in consequence, the thickness of the interface remains smaller. In figure 11*b*, $Ra_e = 54\,141$ corresponding to $E_a = 100\,000\ \mathrm{V\,m^{-1}}$ has the least thickness, and the largest gradient is maintained over the course of simulation owing to stronger electroviscous force. Consequently, faster growth of instability at such higher electric

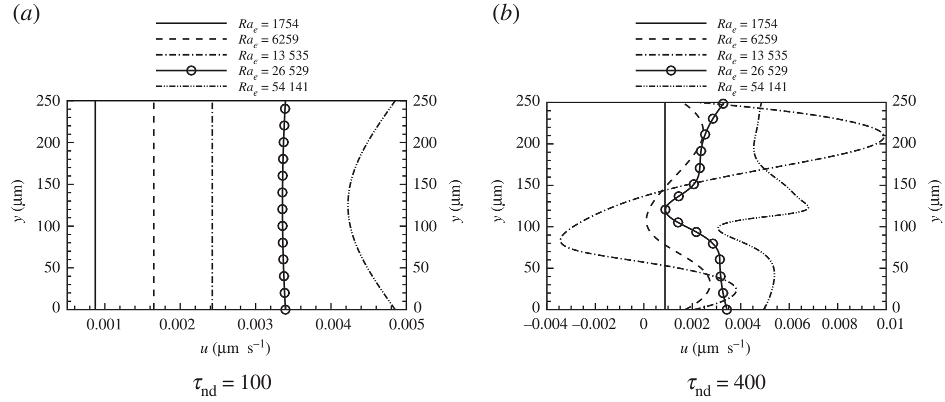

Figure 11. Convection at the boundary and electroviscous effects in the bulk. Plots represent stream-wise velocity in m s^{-1} at a cross-section 200 μm away from the inlet. (*a*) $\tau_{\rm nd} = 100$, (*b*) $\tau_{\rm nd} = 400$.

fields is observed in the contour plots in figure 10. However, in figure 11, we observe a plug-like velocity profile for $Ra_e = 1754$ at both $\tau_{\rm nd} = 100$ and 400. Since, at $Ra_e = 1754$, molecular diffusion is dominant over electroviscous effects, only the electroconvection due to slip at the boundary is reflected in this velocity profile.

In figure 12, we present the maximum cross-stream velocity as a function of time. In figure 12, we observe a sharper gradient of velocity with increasing electric fields. Such an increase in the gradient of cross-stream velocity indicates the higher growth rate of instability corresponding to stronger electric fields. Consequently, we observe that the velocity profile corresponding to $E_a = 18\,000\ \mathrm{V\,m^{-1}}$ has the least slope and saturates at a value of the order of $10^{-6}\ \mathrm{m\,s^{-1}}$ owing to high molecular diffusion. In contrast, while for electric fields $E_a = 34\,000$–$120\,000\ \mathrm{V\,m^{-1}}$, velocity exponentially increases to a peak, for $E_a = 120\,000\ \mathrm{V\,m^{-1}}$ we observe the highest slope in velocity owing to stronger electroviscous effects. Figure 13 shows the variation in non-dimensional maximum cross-stream velocity as a function of dimensionless time for different Ra_e values from the present simulations and the results obtained from Lin's model. Here, velocity and time are scaled using electroviscous velocity ($U_{\rm ev}$) and electroviscous time ($\tau_{\rm ev}$), respectively. As observed in figure 13, because of electroviscous scaling, the normalized velocity profiles align themselves to an exponentially increasing single curve for a range of $Ra_e = 6259$–$77\,962$. However, the velocity profile for $Ra_e = 1754$ does not grow at the same rate and deviates from the collapsing curve. Such a deviation implies that the stabilizing effects of molecular diffusion nullify the destabilizing electroviscous effects at low Ra_e, which agrees with our previous conclusion that higher molecular diffusion at $Ra_e = 1754$ suppresses the instabilities. Hence, electroviscous scaling becomes invalid for electric fields below this threshold. We further observe in figure 13 that the peak non-dimensional velocity and the corresponding non-dimensional time are the same for the present simulations and Lin's simulations, thus implying that the present hybrid model is capturing the same physics.

However, in figure 13, we observe insignificantly lower initial velocity than Lin's numerical simulations [9]. Higher numerical diffusion due to $\tau_{D_{\rm eff}}$ along with deviation in the non-dimensional concentration difference ($\delta C_0/C_0$) leads to such a deviation in the initial normalized maximum velocity between the two models. For example, $\delta C_0/C_0$ corresponding to $Ra_e = 54\,141$ is of the order of 10^{-5} in simulations by Lin *et al.* [9] and is calculated from $\delta C_0/C_0 = \epsilon E_0/FC_0H$. However, in the present calculations, it is of the order of 10^{-4}, leading to a stronger electroviscous force. In consequence, initially after application of the electrical body force, a higher diffusion appears. Such a higher diffusion, along with the aforementioned reason, leads to the smaller initial velocity. Furthermore, the higher electroviscous force accelerates the instability mechanism, causing the collapsing curve to be steeper in the present hybrid simulations than in the DNS.

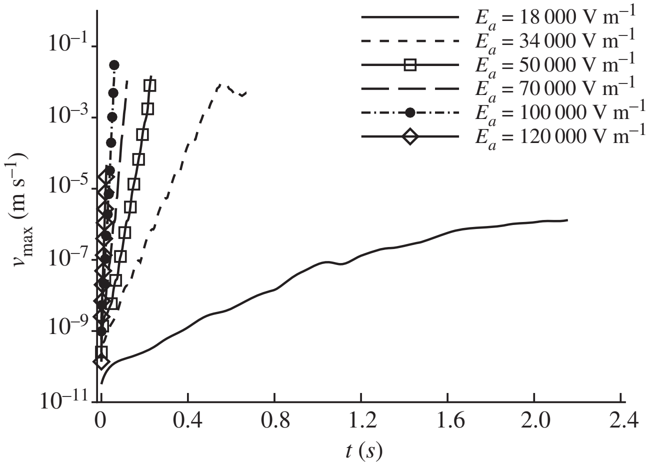

Figure 12. Plot for dimensional v_{max} as a function of time t at different electric fields. v_{max} is the maximum cross-stream velocity at certain time steps in the field obtained from the present 2D hybrid LB-FD simulations. The figure depicts velocities corresponding to electric fields $E_a = 18\,000$ (solid line), 34 000 (dashed line), 50 000 (solid line with open squares), 70 000 (long dashed line), 100 000 (dash-dotted line with filled circles) and 120 000 (solid line with open diamonds) V m^{-1}.

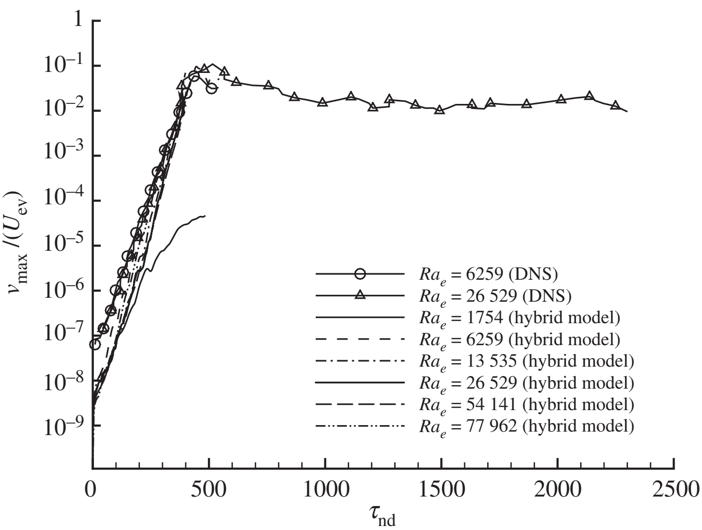

Figure 13. Plot of non-dimensional velocity as a function of non-dimensional time, showing the validity of the present model by comparing electroviscous scaling and its validation at different electric fields. In this plot, all the non-dimensional velocities collapse to a single curve except for $Ra_e = 1754$, which is in agreement with the results from Lin *et al.* (The results from DNS are reproduced from Lin *et al.* [9], with the permission of AIP Publishing.)

5. Conclusion

In this work, we have developed a 2D hybrid LB-FD model for the numerical simulation of EK flows. Ohmic model equations for binary electrolytes were solved under a thin EDL assumption while using LBM for fluid transport and the electrical conductivity equation, and FDM for the Ohmic current conservation equation. The numerical framework developed couples three equations with different time scales to study the steady and transient EK flows. The results obtained from the present simulations agree with the results from previous studies, both qualitatively and quantitatively. In comparison with analytical results for EOF with a sinusoidally variable ζ-potential, our model predicts the flows with an error within 10%. Such a result quantitatively validates our model for steady EOF. The similitude between streamlines and electric field lines and the comparison of conductivity contours with simulations by Lin *et al.* [9] provide qualitative validity of our model for EOF and EK instability, respectively. These contours also provide qualitative validity of electroviscous effects and predict an instability regime with reasonable accuracy. Dimensional and normalized velocity plots for EK instability prove the quantitative validation of the present hybrid model for predicting transient EK flows. Further, they show the efficiency of our model in capturing electroviscous physics. Overall, numerical predictions from the present model indicate that this model is capable of simulating transient EK flows with expected accuracy under a thin EDL condition. While our model is capable of capturing the onset of the instability mechanism in EK instability, it is unstable at the mixing regime for higher Ra_e ($Ra_e > 6259$). An MRT scheme for fluid transport and an unconditionally stable scheme such as hopscotch for Ohm's law can be adapted to overcome the unstable nature. An extension to the study of multiphase EHDs along with the aforementioned adaptation can be considered as a future scope of this study.

Data accessibility. Data are provided as the electronic supplementary material.

Authors' contributions. H.S.B. carried out the model development and performed the data analysis. S.K. and S.S.B. conceived of and designed the study. H.S.B. and S.S.B. drafted the manuscript. All authors read and approved the manuscript. All authors agree to be held accountable for the work performed therein.

Competing interests. We declare that we have no competing interests.

Funding. S.K. and S.S.B. acknowledge the financial support received from the Department of Science and Technology (DST), India (grant no. IMP/2018/000422). S.K. acknowledges the financial support received from the Department of Science and Technology (DST), India (grant no. IFA12-ENG-15).

Acknowledgements. The authors would like to thank the anonymous referees for their pertinent remarks and insightful questions.

References

1. Levich V. 1962 *Physicochemical hydrodynamics*, 2nd edn. Englewood Cliffs, NJ: Prentice Hall.
2. Laser DJ, Santiago JG. 2004 A review of micropumps. *J. Micromech. Microeng.* **14**, R35–R64. (doi:10.1088/0960-1317/14/6/R01)
3. Bahga SS, Vinogradova OI, Bazant MZ. 2010 Anisotropic electro-osmotic flow over super-hydrophobic surfaces. *J. Fluid Mech.* **644**, 245–255. (doi:10.1017/S0022112009992771)
4. Herr AE, Molho JI, Santiago JG, Mungal MG, Kenny TW, Garguilo MG. 2000 Electroosmotic capillary flow with nonuniform zeta potential. *Anal. Chem.* **72**, 1053–1057. (doi:10.1021/ac990489i)
5. Bharadwaj R, Santiago JG, Mohammadi B. 2002 Design and optimization of on-chip capillary electrophoresis. *Electrophoresis* **23**, 2729–2744. (doi:10.1002/1522-2683(200208)23:16 <2729::AID-ELPS2729>3.0.CO;2-I)
6. Ramos A. 2011 *Electrokinetics and electrohydrodynamics in microsystems*. CISM International Centre for Mechanical Sciences, vol. 530. New York, NY: Springer.
7. Hoburg JF, Melcher JR. 1976 Internal electrohydrodynamic instability and mixing of fluids with orthogonal field and conductivity gradients. *J. Fluid Mech.* **73**, 333–352. (doi:10.1017/S0022112076001390)
8. Melcher JR, Schwarz WJ. 1968 Interfacial relaxation overstability in a tangential electric field. *Phys. Fluids* **11**, 2604–2616. (doi:10.1063/1.1691866)
9. Lin H, Storey BD, Oddy MH, Chen CH, Santiago JG. 2004 Instability of electrokinetic microchannel flows with conductivity gradients. *Phys. Fluids* **16**, 1922–1935. (doi:10.1063/1.1710898)
10. Chen CH, Santiago JG. 2002 Electrokinetic flow instability in high concentration gradient microflows. In *Proc. ASME 2002 Int. Mechanical Engineering Congress and Exposition, Fluids Engineering, New Orleans, LA, 17–22 November 2002*, pp. 415–418. New York, NY: ASME.
11. Chen CH, Lin H, Lele SK, Santiago JG. 2005 Convective and absolute electrokinetic instability with conductivity gradients. *J. Fluid Mech.* **524**, 263–303. (doi:10.1017/S0022112004002381)

12. Posner JD, Santiago JG. 2006 Convective instability of electrokinetic flows in a cross-shaped microchannel. *J. Fluid Mech.* **555**, 1–42. (doi:10.1017/S0022112005008542)
13. Posner JD, Pérez CL, Santiago JG. 2012 Electric fields yield chaos in microflows. *Proc. Natl Acad. Sci. USA* **109**, 14353–14356. (doi:10.1073/pnas.1204920109)
14. Patankar NA, Hu HH. 1998 Numerical simulation of electroosmotic flow. *Anal. Chem.* **70**, 1870–1881. (doi:10.1021/ac970846u)
15. Oddy MH, Santiago JG, Mikkelsen JC. 2001 Electrokinetic instability micromixing. *Anal. Chem.* **73**, 5822–5832. (doi:10.1021/ac0155411)
16. Dubey K, Gupta A, Bahga SS. 2017 Coherent structures in electrokinetic instability with orthogonal conductivity gradient and electric field. *Phys. Fluids* **29**, 092007. (doi:10.1063/1.5003409)
17. Sharan S, Gupta P, Bahga SS. 2017 Mechanism of electrohydrodynamic instability with collinear conductivity gradient and electric field. *Phys. Rev. E* **95**, 023103. (doi:10.1103/PhysRevE.95.023103)
18. Gaur R, Bahga SS. 2017 Electrohydrodynamic instability of ion-concentration shock wave in electrophoresis. *Phys. Rev. E* **95**, 063109. (doi:10.1103/PhysRevE.95.063109)
19. Santos JJ, Storey BD. 2008 Instability of electro-osmotic channel flow with streamwise conductivity gradients. *Phys. Rev. E* **78**, 046316(1)–046316(10).
20. Lindken R, Rossi M, Große S, Westerweel J. 2009 Micro-particle image velocimetry (μPIV): recent developments, applications, and guidelines. *Lab Chip* **9**, 2551–2567. (doi:10.1039/b906558j)
21. Bianchi F, Ferrigno R, Girault HH. 2000 Finite element simulation of an electroosmotic-driven flow division at a T-junction of microscale dimensions. *Anal. Chem.* **72**, 1987–1993. (doi:10.1021/ac991225z)
22. Yang RJ, Fu LM, Hwang CC. 2001 Electroosmotic entry flow in a microchannel. *J. Colloid Interface Sci.* **244**, 173–179. (doi:10.1006/jcis.2001.7847)
23. Dutta P, Beskok A, Warburton TC. 2002 Numerical simulation of mixed electroosmotic/pressure driven microflows. *Numer. Heat Transfer, Part A: Appl.* **41**, 131–148. (doi:10.1080/104077802317221366)
24. Storey BD. 2005 Direct numerical simulation of electrohydrodynamic flow instabilities in microchannels. *Physica D* **211**, 151–167. (doi:10.1016/j.physd.2005.08.010)
25. Luo WJ. 2009 Effect of ionic concentration on electrokinetic instability in a cross-shaped microchannel. *Microfluid. Nanofluid.* **6**, 189–202. (doi:10.1007/s10404-008-0316-2)
26. Li Q, Delorme Y, Frankel SH. 2016 Parametric numerical study of electrokinetic instability in cross-shaped microchannels. *Microfluid. Nanofluid.* **20**, 29–41. (doi:10.1007/s10404-015-1666-1)
27. Hlushkou D, Kandhai D, Tallarek U. 2004 Coupled lattice-Boltzmann and finite-difference simulation of electroosmosis in microfluidic channels. *Int. J. Numer. Methods Fluids* **46**, 507–532. (doi:10.1002/fld.765)
28. Melchionna S, Succi S. 2005 Lattice Boltzmann–Poisson method for electrorheological nanoflows in ion channels. *Comput. Phys. Commun.* **169**, 203–206. (doi:10.1016/j.cpc.2005.03.045)
29. Wang M, Kang Q. 2010 Modeling electrokinetic flows in microchannels using coupled lattice Boltzmann methods. *J. Comput. Phys.* **229**, 728–744. (doi:10.1016/j.jcp.2009.10.006)
30. Yoshida H, Kinjo T, Washizu H. 2014 Coupled lattice Boltzmann method for simulating electrokinetic flows: a localized scheme for the Nernst–Plank model. *Commun. Nonlinear Sci. Numer. Simul.* **19**, 3570–3590. (doi:10.1016/j.cnsns.2014.03.005)
31. Patil DV, Premnath KN, Banerjee S. 2014 Multigrid lattice Boltzmann method for accelerated solution of elliptic equations. *J. Comput. Phys.* **265**, 172–194. (doi:10.1016/j.jcp.2014.01.049)
32. Sukop MC, Thorne Jr DT. 2006 *Lattice Boltzmann modeling: an introduction for geoscientists and engineers*. Berlin, Germany: Springer-Verlag.
33. Mohamad AA. 2011 *Lattice Boltzmann method: fundamentals and engineering applications with computer codes*. London, UK: Springer-Verlag.
34. Succi S. 2001 *The lattice Boltzmann equation for fluid dynamics and beyond*. Numerical Mathematics and Scientific Computation. New York, NY: Oxford University Press.
35. Rosso M, Chazalviel JN, Chassaing E. 2006 Calculation of the space charge in electrodeposition from a binary electrolyte. *J. Electroanal. Chem.* **587**, 323–328. (doi:10.1016/j.jelechem.2005.11.030)
36. Rosso M. 2007 Electrodeposition from a binary electrolyte: new developments and applications. *Electrochim. Acta* **53**, 250–256. (doi:10.1016/j.electacta.2007.02.026)

37. He X, Chen S, Doolen GD. 1998 A novel thermal model for the lattice Boltzmann method in incompressible limit. *J. Comput. Phys.* **146**, 282–300. (doi:10.1006/jcph.1998.6057)
38. Yoshida H, Nagaoka M. 2010 Multiple-relaxation-time lattice Boltzmann model for the convection and anisotropic diffusion equation. *J. Comput. Phys.* **229**, 7774–7795. (doi:10.1016/j.jcp.2010.06.037)
39. Chai Z, Zhao TS. 2013 Lattice Boltzmann model for the convection-diffusion equation. *Phys. Rev. E* **87**, 063309(1)–063309(15). (doi:10.1103/PhysRevE.87.063309)
40. Li L, Mei R, Klausner JF. 2013 Boundary conditions for thermal lattice Boltzmann equation method. *J. Comput. Phys.* **237**, 366–395. (doi:10.1016/j.jcp.2012.11.027)
41. Schwartzentruber T, Boyd I. 2005 Detailed analysis of a hybrid CFD-DSMC method for hypersonic non-equilibrium flows. In *Proc. 38th AIAA Thermophysics Conf., Toronto, Ontario, Canada, 6–9 June 2005*, pp. 1–12. Reston, VA: American Institute of Aeronautics and Astronautics.
42. Xiao H, Sun J. 2011 Algorithms in a robust hybrid CFD-DEM solver for particle-laden flows. *Commun. Comput. Phys.* **9**, 297–323. (doi:10.4208/cicp.260509.230210a)
43. Esfahanian V, Pour AS, Harsini I, Haghani A, Pasandeh R, Shahbazi A, Ahmadi G. 2013 Numerical analysis of flow field around NREL phase II wind turbine by a hybrid CFD/BEM method. *J. Wind Eng. Ind. Aerodyn.* **120**, 29–36. (doi:10.1016/j.jweia.2013.06.006)
44. Castellani F, Burlando M, Taghizadeh S, Astolfi D, Piccioni E. 2014 Wind energy forecast in complex sites with a hybrid neural network and CFD based method. *Energy Procedia* **45**, 188–197. (doi:10.1016/j.egypro.2014.01.021)
45. Farhat H, Celiker F, Singh T, Lee JS. 2011 A hybrid lattice Boltzmann model for surfactant-covered droplets. *Soft Matter* **7**, 1968–1985. (doi:10.1039/c0sm00569j)
46. Kondaraju S, Farhat H, Lee JS. 2012 Study of aggregational characteristics of emulsions on their rheological properties using the lattice Boltzmann approach. *Soft Matter* **8**, 1374–1384. (doi:10.1039/C1SM06193C)
47. Hasan WF, Farhat H, Kondaraju S, Singh T. 2018 Hybrid quasi-steady thermal lattice Boltzmann model for studying the rheology of surfactants contaminated emulsions. *Comput. Fluids* **165**, 188–198. (doi:10.1016/j.compfluid.2018.01.017)
48. Lin H. 2009 Electrokinetic instability in microchannel flows: a review. *Mech. Res. Commun.* **36**, 33–38. (doi:10.1016/j.mechrescom.2008.07.012)
49. Melcher JR. 1981 *Continuum electromechanics*. Cambridge, MA: MIT Press.
50. Yagub A, Farhat H, Kondaraju S, Singh T. 2015 A lattice Boltzmann model for substrates with regularly structured surface roughness. *J. Comput. Phys.* **301**, 402–414. (doi:10.1016/j.jcp.2015.08.040)
51. Krüger T, Kusumaatmaja H, Kuzmin A, Shardt O, Silva G, Viggen EM. 2017 *The lattice Boltzmann method: principles and practice*. New York, NY: Springer.
52. Anderson D, Pletcher RH, Tannehill JC. 2012 *Computational fluid mechanics and heat transfer*, 3rd edn. Washington, DC: CRC Press.
53. Zou Q, He X. 1997 On pressure and velocity boundary conditions for the lattice Boltzmann BGK model. *Phys. Fluids* **9**, 1591–1598. (doi:10.1063/1.869307)
54. Ajdari A. 1995 Electro-osmosis on inhomogeneously charged surfaces. *Phys. Rev. Lett.* **75**, 755–758. (doi:10.1103/PhysRevLett.75.755)
55. Ajdari A. 1996 Generation of transverse fluid currents and forces by an electric field: electro-osmosis on charge-modulated and undulated surfaces. *Phys. Rev. E* **53**, 4996–5005. (doi:10.1103/PhysRevE.53.4996)
56. Devasenathipathy S, Santiago JG, Takehara K. 2002 Particle tracking techniques for electrokinetic microchannel flows. *Anal. Chem.* **74**, 3704–3713. (doi:10.1021/ac011243s)
57. Melcher JR, Taylor GI. 1969 Electrohydrodynamics: a review of the role of interfacial shear stresses. *Annu. Rev. Fluid Mech.* **1**, 111–146. (doi:10.1146/annurev.fl.01.010169.000551)
58. Kirby B. 2010 *Micro- and nanoscale fluid mechanics: transport in microfluidic devices*. New York, NY: Cambridge University Press.